A Radiative Model of the Stable Nocturnal Boundary Layer with Application to the Polar Night

TODD A. CERNI[1] AND THOMAS R. PARISH

Department of Atmospheric Science, University of Wyoming, Laramie, WY 82071

(Manuscript received 4 April 1984, in final form 16 August 1984)

ABSTRACT

A graybody, longwave, radiative transfer model based on revised estimates of the absorption characteristics of CO_2 and H_2O is proposed. The model is computationally efficient and is designed for use within larger mesoscale primitive equation models. Tests have shown that the graybody model accurately simulates atmospheric heating rates as predicted by more detailed radiation models. When incorporated within a simple one-dimensional model, the radiation parameterization provides realistic simulations of the strong temperature inversion over the interior of Antarctica in winter.

1. Introduction

During nocturnal conditions the longwave radiative exchanges between the atmosphere and surface are important components of the energy budget of the lower troposphere. In cases where little or no cloud cover exists, the net longwave flux divergence at the surface results in a large cooling rate which, at least in the initial stages of nocturnal boundary layer development, overwhelms the turbulent heat fluxes within both the atmospheric surface boundary layer (SBL) and lower planetary boundary layer (PBL). It is clear that proper specification and evolution of the terrestrial and atmospheric radiative fluxes requires a knowledge of the absorption and emission characteristics of the atmosphere. In particular, the absorption and emission are sensitive to the vertical profiles of water vapor and temperature. True representation of radiative cooling is of central importance in understanding certain dynamic features of the nocturnal boundary layer, especially gravity-driven slope flows such as mountain–valley circulations or katabatic winds. The purpose of this paper is to offer a relatively economical graybody radiative transfer scheme for simulating the longwave radiation budget. The scheme is intended for use in mesoscale numerical models. Care has been taken to incorporate emissivities for both water vapor (H_2O) and carbon dioxide (CO_2) based on recent work (Liou and Ou, 1981, 1983; Ou and Liou, 1983).

The handling of longwave radiation processes in current mesoscale models varies widely depending on the particular type and scale of motion under consideration. Certain models incorporate a relatively complete graybody treatment while in other cases the longwave radiative transfer is less important and often ignored. Anthes (1983) has reviewed a number of the widely used operational and research models and lists for each the type of schemes used in parameterizing subgrid-size processes. He notes that for the majority of short-range model forecasts, the most important radiative effect is simply absorption of solar radiation at the surface. Most models listed in the paper have no explicit radiation scheme. An example of a relatively detailed graybody approach to longwave radiation simulation appears in Mahrer and Pielke (1977) and McNider and Pielke (1981). Both works are based on the emissivity functions of Sasamori (1968, 1972).

2. Infrared radiative transfer

Longwave radiative transfer can be modeled by a number of schemes. These schemes all fall into three general categories: line-by-line calculations, band models and graybody models. The basic trade-off involved in choosing between these three classes of models is one of accuracy versus computational speed and simplicity. The models that are based on line-by-line calculations are inherently the most accurate, but are awesome in terms of computational requirements. Band models require that the longwave infrared spectrum be divided into a large number of bands with a spectrally averaged transmission for each band. Band transmissivities are obtained either from analytical band models or from smoothing of experimentally measured transmission functions. Band models represent a medium compromise in both accuracy and computational speed and are the most popular choice for detailed radiation studies. Graybody models

[1] Current affiliation: Ophir Corporation, Lakewood, CO 80235.

assume that each atmospheric layer can be represented by a single transmissivity, which has been weighted by the Planck function and averaged over all wavelengths. While this class of models makes some compromises in accuracy, the loss in accuracy is small in terms of total energy budget considerations. Furthermore, it is the only class of model with sufficient computational speed to be realistically considered for inclusion in primitive equation models, climate models and other comprehensive atmospheric models. Hence, a graybody radiative transfer model that makes use of the most recently derived graybody transmissivities will be used in this study to model the nocturnal boundary layer.

Solutions to the equation of radiative transfer for upward and downward propagating radiation, assuming no atmospheric scattering and local thermodynamic equilibrium, can be written

$$F\uparrow(u) = \sigma T_s^4 t(u, T_s) + \int_0^u \sigma T^4(u') \frac{dt(u - u', T)}{du'} du', \tag{1}$$

$$F\downarrow(u) = \int_{u_t}^u \sigma T^4(u') \frac{dt(u' - u, T)}{du'} du' \tag{2}$$

(see Liou, 1980). The upward and downward propagating flux densities, in units of W m^{-2}, are written $F\uparrow$ and $F\downarrow$, respectively; σ is the Stefan-Boltzmann constant, T the temperature, T_s the surface temperature, u the amount of absorbing gas in g cm^{-2} and t the graybody flux transmission function. The derivation of (1) and (2) makes use of the assumption that the flux transmission function can be simply evaluated from the transmission function through introduction of a diffusivity factor (Rodgers and Walshaw, 1966). Also, the lower boundary has been taken to be a blackbody that radiates at T_s.

If the graybody emissivity is substituted for the transmission with

$$\epsilon(u, T) = 1 - t(u, T), \tag{3}$$

then the solutions can be written in the form

$$F\uparrow(u) = \sigma T^4[1 - \epsilon(u, T_s)] + \int_u^0 \sigma T^4(u') d\epsilon(u - u', T), \tag{4}$$

$$F\downarrow(u) = \int_u^{u_t} \sigma T^4(u') d\epsilon(u' - u, T). \tag{5}$$

Equations (4) and (5) serve as the basis of the radiative transfer model used in this study.

Since T as a function of u cannot generally be described in terms of an analytic function, the integrals in (4) and (5) must be evaluated numerically. The first term in (4) represents the attenuated surface emission reaching level u, while the second term represents the summation of atmospheric emission from all layers beneath level u. The downward propagating flux at level u (5) is the summation of atmospheric emission from all layers above level u. The physical interpretation of the integrals in (4) and (5) is that each layer contributes to the atmospheric emission according to the product of its blackbody flux density and the differential emissivity for that layer. Since the differential emissivity is a function of $u - u'$ and the emissivity functions are approximately proportional to log u (see Figs. 1 and 2), the layer adjacent to level u will tend to make the largest contribution to the atmospheric emission reaching level u. Also the contribution per layer tends to decrease proportional to the distance from level u.

Graybody emissivities were first introduced by Elsasser (1942) and were based on analytical band model calculations. These values have since been superseded as more accurate band models became available. The graybody emissivities of Sasamori (1968) and Staley and Jurica (1970) have tended to be the most heavily used in radiative transfer modeling. However, since the values of Sasamori (1968) are based on the work of Yamamoto (1952) and the values of Staley and Jurica (1970) are based on the work of Elsasser and Culbertson (1960), there would appear to be room for improvement if one were to generate graybody emissivities based upon more recent theoretical and experimental work.

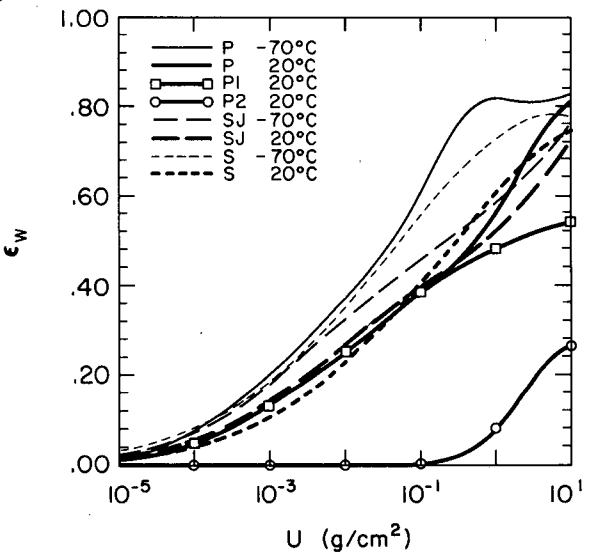

FIG. 1. Emissivities for water vapor versus H_2O amount at two temperatures. The P1 and P2 represent results ϵ_{w1} and ϵ_{w2} from the present study, while P represents the sum of ϵ_{w1} and ϵ_{w2}. The SJ represents the total H_2O emissivity, to include all bands and the H_2O–CO_2 overlap, from Staley and Jurica (1970). The S represents the total H_2O emissivity from Sasamori (1968). The H_2O–CO_2 overlap contribution for the S and SJ curves were calculated assuming a CO_2 amount of 0.1 g cm^{-2} for comparison with the P curves for which the overlap contribution is independent of CO_2 amount.

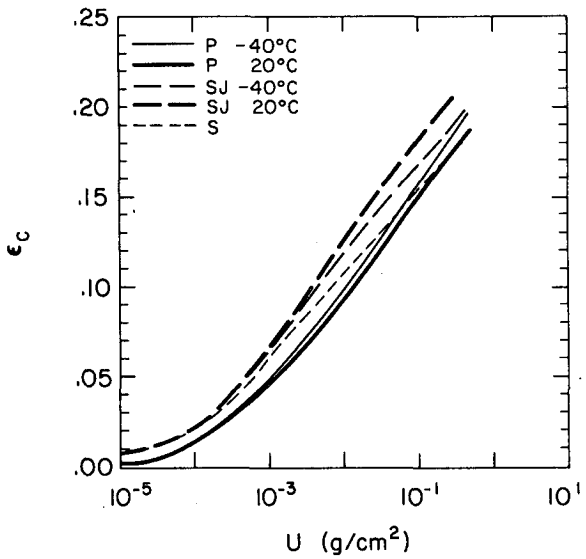

FIG. 2. Emissivities for carbon dioxide versus CO_2 amount at two temperatures. The P, SJ and S represent the same authors as in Fig. 1. The ϵ_c for S is independent of temperature.

Graybody emissivities incorporated in this model are based on the work of Liou and Ou (1981, 1983) and Ou and Liou (1983). The present model uses emissivities of water vapor based on work from the first two references and an emissivity for carbon dioxide based on work from the latter reference. Ozone has not been included in this model, as the model is intended only for tropospheric applications, where ozone's contribution is negligible. Liou and Ou[2] have derived graybody emissivities for the 14.7 μm CO_2 band and one each for the 6.3 μm H_2O band, the 13–1000 μm H_2O band, the H_2O continuum and the H_2O–CO_2 overlap as a function of corrected absorber amount $\bar{u}$ and temperature. The emissivities for water vapor are expressed as third-order polynomials in $\bar{u}$ at a few temperatures, with interpolation required at intermediate temperatures. The absorber amounts were corrected for both temperature and pressure. The emissivity for carbon dioxide is expressed in terms of an integral of the Planck function with temperature and pressure corrections to the absorber amount.

The graybody emissivities proposed by Liou and Ou are functionally far more complicated and computationally far more lengthy than those of Sasamori (1968). This burden makes them difficult to include in a model that involves a considerable amount of atmospheric dynamics and that includes temporal evolution of the atmosphere. It is proposed that the emissivities derived by Liou and Ou can be functionally simplified and computationally shortened without significant loss of accuracy for tropospheric work. It is proposed that the emissivity of water vapor be expressed as one function in $\bar{u}$ and T for both bands and the overlap, with a pressure-corrected absorber amount, plus a second function in $\bar{u}$ and T for the continuum, with a vapor pressure-corrected absorber amount. The emissivity for CO_2 will be expressed as a single function in $\bar{u}$ and T, with a pressure-corrected absorber amount. For CO_2 the emissivity used in this model is

$$\epsilon_c = (1.0 - |0.005T - 1.250|^{1.85}) \times (0.2167 + 0.05505 \log\bar{u}_c - 0.004189 \log^2\bar{u}_c - 0.001328 \log^3\bar{u}_c), \quad (6)$$

$$\bar{u}_c = \int_0^{u_c} \frac{P}{P_0}\, du, \quad \bar{u}_c \geq 10^{-5} \text{ g cm}^{-2}, \quad (7)$$

where T is in K, P is the atmospheric pressure and P_0 is 1 atm. The single emissivity that represents the 6.3 μm H_2O band, the 13–1000 μm H_2O band and the H_2O–CO_2 overlap is

$$\epsilon_{w1} = (0.7065 + 0.1431 \log\bar{u}_{w1} - 0.02228 \log^2\bar{u}_{w1} - 0.004653 \log^3\bar{u}_{w1}) \times (3.224 \log^2 T - 17.242 \log T + 23.62)^{1.0+0.10|\log\bar{u}_{w1}+1.0|}, \quad (8)$$

$$\bar{u}_{w1} = \int_0^{u_w} \frac{P}{P_0}\, du, \quad \bar{u}_{w1} \geq 10^{-5} \text{ g cm}^{-2}. \quad (9)$$

The emissivity that represents the H_2O continuum is

$$\epsilon_{w2} = (0.8132 \log T - 1.741) \times \exp\left\{-\left(\frac{\log\bar{u}_{w2} - 8.892 \log T + 20.85}{1.597 \log T - 2.950}\right)^2\right\}, \quad (10)$$

$$\bar{u}_{w2} = \int_0^{u_w} \frac{e}{e_0}\, du, \quad \bar{u}_{w2} \geq 10^{-5} \text{ g cm}^{-2}, \quad (11)$$

where e is the vapor pressure due to H_2O and e_0 is the saturation vapor pressure at 296 K. Then the total emissivity ϵ, required in (4) and (5), is simply the sum of ϵ_c, ϵ_{w1} and ϵ_{w2}. It should be noted that while ϵ_c and ϵ_{w1} are functional fits to the emissivities developed by Liou and Ou, ϵ_{w2} was developed with an additional physical constraint in mind. The physical constraint is that ϵ should not exceed 1.0. The combined emissivities developed by the aforementioned authors exceed unity for $u_w \geq 1.0$ g cm^{-2}. This error may be due to overlap between the 13–1000 μm H_2O band the H_2O continuum, which was implied by the work of Roberts *et al.* (1976), but not explicitly included in the graybody emissivity formulation. In the present study, ϵ_{w2} has been reduced

[2] When using the tabulated coefficients from Table 1 of Liou and Ou (1983), one must be aware of certain errors. The coefficients for the 6.3 μm H_2O (vibrational–rotational) band and the H_2O continuum have been interchanged. Also, the $a_{3,4}$ coefficients are of the wrong sign.

such that ϵ would not exceed unity. Furthermore, temperature corrections to $\bar{u}_c$ and $\bar{u}_{w1}$ have been dropped in this formulation as being not significant, while the large temperature dependence of $\bar{u}_{w2}$ on T has been included as part of the temperature dependence of ϵ_{w2}.

Figures 1 and 2 show comparisons between emissivities developed in the present study and those of Sasamori (1968) and Staley and Jurica (1970). The total water emissivities (Fig. 1) at −70°C agree well for $u \leqslant 3 \times 10^{-3}$ g cm^{-2}, but seriously diverge at large values of u. At that point, the emissivities derived in the present study become the greatest and those of Staley and Jurica (1970) become the smallest. The total water emissivities from all authors show a decrease at warmer temperatures, which is caused by the dominant temperature dependency of the 13–1000 μm band. The narrowing of the difference between −70 and 20°C total water emissivities at large u, shown by all authors, is caused by the temperature dependence of the continuum that has its largest contribution at warm temperatures and large u. The temperature extremes chosen for displaying the CO_2 emissivity (Fig. 2) were only −40–20°C because (6) yields about the same value of ϵ_c for both −70 and 20°C. Figure 2 shows that the CO_2 emissivity derived in the present study is lower than that of other authors for $u \leqslant 0.05$ g cm^{-2}, and then comes into close agreement with the temperature-independent curve of Sasamori (1968). One can conclude from Figs. 1 and 2 that emissivities derived in the present study are closest to those of Sasamori (1968) and are very close over a limited range of u and T.

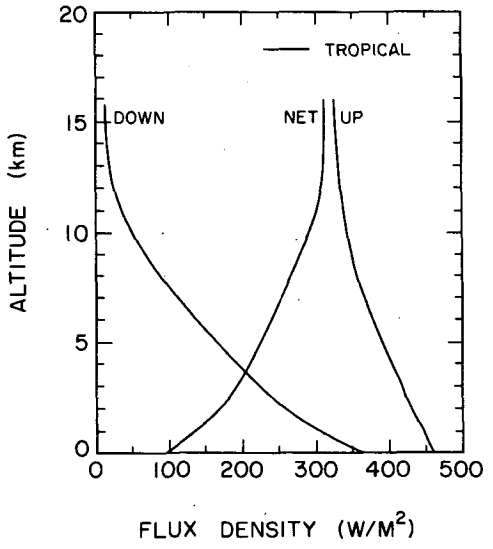

FIG. 3. Up, down and net flux densities versus altitude for a tropical atmospheric profile. The tropical profile was taken from McClatchey *et al.* (1972).

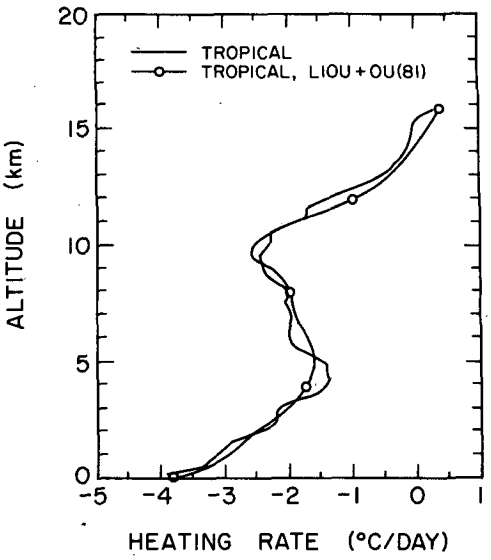

FIG. 4. Atmospheric heating rates versus altitude for a tropical atmospheric profile. The tropical profile was as in Fig. 3. The curve with circles is from Liou and Ou (1981) and the result of a multiple band model, while the curve without circles is from the present study and the result of a graybody model.

The graybody radiative transfer model prescribed by (4) and (5) and incorporating the emissivities (6), (8) and (10) is a rather efficient scheme for inclusion in detailed numerical models, and compares favorably in accuracy with more detailed radiative transfer models. Figure 3 displays calculated flux densities for a tropical atmosphere, and Fig. 4 displays the corresponding atmospheric heating rates. The heating rates were calculated by taking differences in net (up minus down) flux densities between the top and bottom of a layer. The results were generated using 48 layers of equal geometric thickness between 0 and 16 km, with a single layer representing the upper atmosphere. The uppermost layer contained the u_c and u_w for the atmosphere above 16 km and was assigned the temperature and pressure corresponding to a level with 0.75 of the pressure at 16 km. Also plotted in Fig. 4 is the heating rate profile reported in Liou and Ou (1981) and calculated from a detailed, multiple band model. The results agree quite well. Some of the differences may be due to differences in vertical resolution and upper boundaries.

Figures 5 and 6 display results of this graybody model for two midlatitude atmospheres, and Figs. 7 and 8 display results for two subarctic atmospheres. Similarities of note in the tropical and two summer atmospheres are the large negative heating rates very close to the surface. This is caused by the shape of the emissivity function for the water vapor continuum and the vapor pressure weighting of $\bar{u}_{w2}$, which results in a rapid decrease of ϵ_{w2} with height. Such results will not be produced by older models that lack a proper formulation of continuum absorption (see

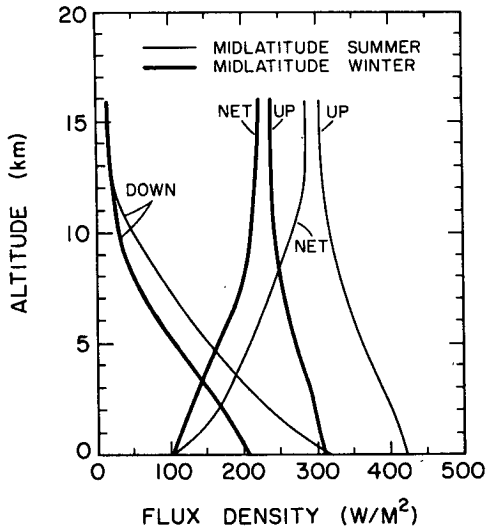

FIG. 5. Up, down and net flux densities versus altitude for two midlatitude atmospheric profiles. The midlatitude profiles were taken from McClatchey *et al.* (1972).

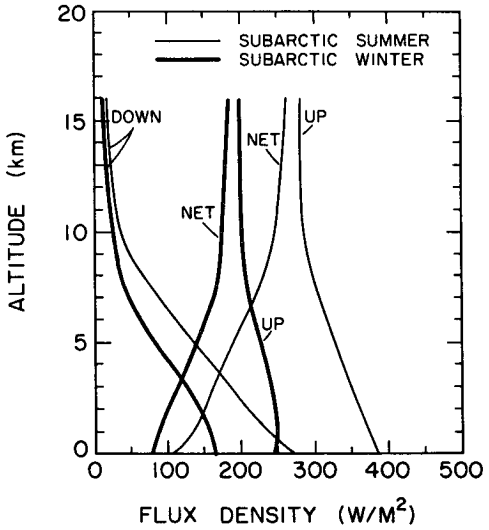

FIG. 7. Up, down and net flux densities versus altitude for two subarctic atmospheric profiles. The subarctic profiles were taken from McClatchey *et al.* (1972).

Roewe and Liou, 1978). The large negative heating rates near the surface are not present in the winter atmospheres because they lack sufficient water vapor for the H_2O continuum (ϵ_{w2}) to play a significant role.

A feature common to all atmospheres is the relative maximum in heating rate near the tropopause, which occurs at 17, 13, 10, 10, and 9 km for the tropical, midlatitude summer, midlatitude winter, subarctic summer and subarctic winter atmospheres, respectively. Of interest in Figs. 3, 5 and 7 are the small differences in net flux at the surface between all five model atmospheres, in spite of large differences in upward and downward propagating fluxes at the surface. Though this is common for model atmospheres (Sasamori, 1968), actual atmospheric soundings can yield substantial differences in surface net flux. The downward propagating fluxes at the surface shown in Fig. 5, for midlatitude winter conditions, are within the range of values given by Sasamori (1968) for measurements of midlatitude winter conditions under cloudless skies.

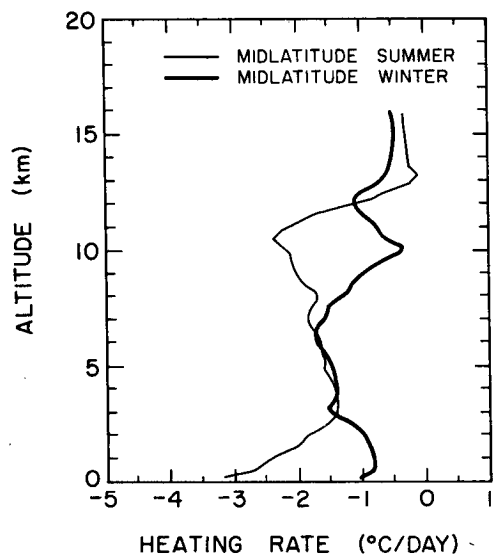

FIG. 6. Atmospheric heating rates versus altitude for the two midlatitude atmospheric profiles of Fig. 5.

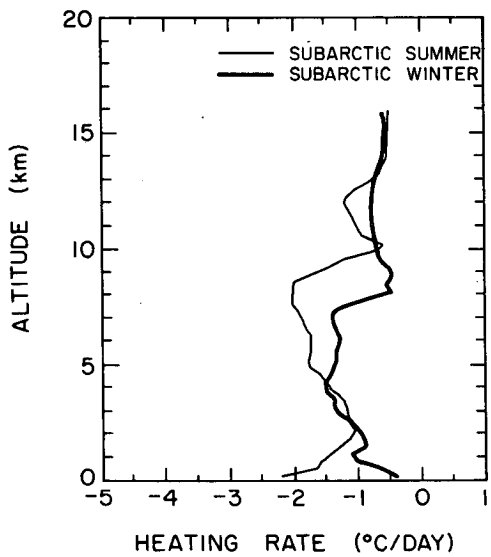

FIG. 8. Atmospheric heating rates versus altitude for the two subarctic atmospheric profiles of Fig. 7.

3. Model simulations of the strong temperature inversion over Plateau Station, Antarctica

a. Plateau Station

During the late 1960s a micrometeorological program was conducted at Plateau Station, Antarctica (79.2°S, 40.5°E) located at an elevation of 3625 m on the high central ridge of East Antarctica. A 32 m tower was constructed with instrumentation to measure wind and temperature at 1, 2, 4, 8, 16, 20, 24 and 32 m. Results of this experiment can be found in Lettau *et al.* (1977), Kuhn *et al.* (1977) and Riordan (1977). The data taken during the austral winter period represent some of the most stable conditions encountered on the planet. The predominant feature of the lower Antarctic atmosphere is the nearly ever-present temperature inversion. Wintertime observations have shown that the inversion strength typically exceeds 20 K and at times approaches 40 K. The strongest increase of temperature with height is found just above the surface and often 75% of the total inversion strength is confined below 50 m. Mahrt and Schwerdtfeger (1970) have used an exponential-shaped temperature profile to simulate the thermal field over the interior of Antarctica. Above the inversion, extending to about 100 m, an isothermal layer is generally present. Representative soundings for sites in interior Antarctica may be found in Schwerdtfeger (1970).

Owing to its position atop the high central ridge and its distance from the highly baroclinic coastal zone, Plateau Station is somewhat sheltered from effects of synoptic disturbances. On occasion, however, the cyclonic influence is able to reach even interior sites and has marked implications on the temperature profile. The downward radiation from low-level cloud cover along with the mixing tendencies of the stronger than average winds, which accompany cyclones, tend to destroy the inversion structure, at times in just a few hours. Plateau Station data often reveal a near isothermal atmosphere from the surface to 100 m during cyclonic storm episodes. Lettau (1966) has given detailed account of rapid SBL temperature changes at South Pole Station resulting from local convergence in the low-level wind field.

b. Model considerations

A series of model experiments have been performed in order to test the ability of the graybody longwave radiation scheme proposed in the previous section to simulate the inversion structure at Plateau Station. As is to be expected, the radiative flux divergence will be shown to be primarily responsible for the inversion development. However, consideration must also be given to the turbulent heat transfer as well as to heat conduction between the surface and deep within the snowpack. The relationship of wind and temperature profiles within the SBL with the turbulent fluxes of heat and momentum has been a topic of study for many years. In particular, expressions relating nondimensional wind shear and temperature gradients to the Monin-Obukhov-Lettau length scale have been proposed by Businger *et al.* (1971) based on data from the Kansas experiment in 1968. Recently, Lettau (1979) has offered modifications to the mathematical forms of Businger *et al.* (1971) resulting in part from evidence for the very stable SBL at South Pole as well as at Plateau Station. For our purposes it is assumed that the similarity expressions of Businger *et al.* (1971) hold within the SBL:

$$\phi_h = 0.74 + 4.7\zeta, \tag{12}$$

$$\phi_m = 1.00 + 4.7\zeta, \tag{13}$$

where ϕ_h is the nondimensional temperature gradient and ϕ_m is the nondimensional wind shear, expressed as

$$\phi_h = \frac{z}{\theta_*}\frac{\partial\theta}{\partial z}, \tag{14}$$

where

$$\theta_* = -\frac{\overline{w'\theta'}}{ku_*},$$

$$\phi_m = \frac{kz}{u_*}\frac{\partial u}{\partial z}. \tag{15}$$

The term ζ is simply z/L where L is the Monin-Obukhov-Lettau length,

$$L = -\theta u_*^3/(kg\overline{w'\theta'}); \tag{16}$$

other symbols have their usual meteorological meaning. Lettau (1979) notes that the top of the SBL can be determined from the shape of Deacon number profiles. Plateau data show the SBL to extend 8–12 m above ground for the stable conditions. In all experiments it is assumed that the SBL is fixed at 8 m. The integrated forms of (12) and (13) are given in Businger (1973).

Above the SBL, the transfer of heat is modeled using K-theory. The thermodynamic prediction equation is expressed

$$\frac{\partial T}{\partial t} = -\frac{1}{\rho}\frac{\partial \rho\overline{w'T'}}{\partial z} + \frac{Q}{c_p}, \tag{17}$$

where Q is the radiative heating rate per unit mass. The flux of heat ($-\overline{w'T'}$) above the SBL is given by

$$-\overline{w'T'} = K\frac{\partial\theta}{\partial z}. \tag{18}$$

Actual K values for the Plateau Station environment have been determined by Kuhn *et al.* (1977). Brost and Wyngaard (1978) have shown these profiles to approximate results obtained from their second-order turbulence model of the stable boundary layer. The

K profile for class 64 from the abovementioned work was assumed representative throughout the evolution of the strong inversion. It should be noted that while this selection is somewhat arbitrary, model runs with slightly different K profiles (classes 44 and 73 from Brost and Wyngaard) yield results nearly identical to the class 64 profile, thereby indicating the model is not particularly sensitive over a range of realistic K values. This again underscores the prime importance of the radiation budget in nocturnal situations.

A final predictive equation required in the model simulation is ground temperature. Use has been made of the force-restore model proposed by Blackadar (1978), which has been shown to give satisfactory results for midlatitude nocturnal boundary layer simulations. The ground temperature equation can be expressed

$$\frac{\partial T_g}{\partial t} = \frac{1}{C_g}(I_A - \sigma T_g^4 - H_0) - K_r(T_g - T_0), \quad (19)$$

where I_A represents the downwelling longwave radiation component from the atmosphere, σT_g^4 the upward radiation (assumed blackbody) from the ground, H_0 the turbulent heat flux carried away from the surface and T_0 refers to the assumed constant temperature of the snow at infinite depth and in model runs is set to 230 K based on subsurface snow temperature measurements made at Plateau Station. Various values of the heat capacity C_g may be found in Anthes and Warner (1978). Here it is assumed that the density of the surface snow layer at Plateau Station is 300 kg m^{-3} (see Radok and Lile, 1977), resulting in a heat capacity value of 5.74×10^4 Jm^{-2} K^{-1}. The relaxation coefficient K_r has been assigned a value of 1.82×10^{-5} s^{-1}, which assumes a periodic heat input period of about four days. Since no solar insolation is present during austral winter months at Plateau Station, the periodic heat input occurs from intrusion of low-level cloudiness and stronger winds associated with cyclones. Power spectra of surface winds at interior sites on the Antarctic continent, presented by Mather and Miller (1966), show a peak near this four-day period, which they attribute to synoptic influence. Sensitivity studies have revealed that the evolution of the ground temperature varies only slightly for a range of relaxation coefficients corresponding to the various estimates of the frequency of cyclone intrusion. The relaxation coefficient chosen for this work seems to best represent the average time scale for which period heat input occurs through atmospheric process during the austral winter.

c. *Model experiments*

Moisture measurements present a problem in very cold environments, such as over Antarctica. As standard practice, the National Weather Service, as well as United States stations in Antarctica, do not report humidity measurements when the dew point drops below −40°C. At Plateau Station and other similarly situated interior stations, the yearly average surface temperatures range between −50 and −60°C. Along the Antarctic coast, yearly average temperatures range between −10 and −20°C. Thus, detailed and accurate moisture profile measurements in Antarctica are limited, and no such measurements have been made at Plateau Station—to our knowledge. However, Schwerdtfeger (1970) notes that a state of supersaturation with respect to ice exists in the surface layer. To check the sensitivity of the graybody radiation scheme to varying degrees of saturation in the Antarctic atmosphere, a series of tests have been conducted in which effects of turbulent heat transfer have been neglected. Thus, the radiative effects are isolated. For each test it is assumed that the relative humidity with respect to ice is 100% in the SBL and drops off exponentially with height to a constant free atmosphere value. The e-folding distance is assumed to be 100 m. Three different free atmosphere relative humidity values have been chosen: 30, 65 and 100%. In each experiment, an isothermal profile (230 K) is assumed to be present in the lowest 1000 m, with a gradual temperature decrease throughout the remaining portion of the troposphere, following the examples in Schwerdtfeger (1970; see his Fig. 13). The radiation model incorporates 24 levels with the highest resolution (8 m) in the lowest 50 m. Each experimental run has been integrated for a total of 24 hours, at which time the major differences arising from the initial relative humidity profiles should be obvious. Figure 9 shows the resulting temperature profiles after the 24-hour integrations. As is instantly seen, the differences in the temperature profiles are remarkably small. Slight differences can be seen in the surface

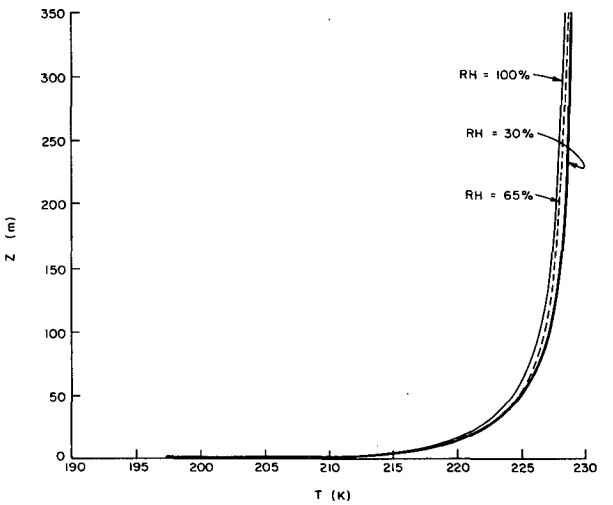

FIG. 9. Resulting temperature profile for varying relative humidities after 24-hour integration period in which only radiative heating effects are considered.

temperature, where more cooling occurs in the 30% free atmosphere relative humidity case, and above 100 m. However, maximum temperature differences between runs vary only by 1 K or so. Introduction of significant gradients in the moisture profile exaggerate such differences only slightly. As discussed earlier, care has been taken to ensure that the graybody approximations yield accurate results for very low water vapor content. Even in the 30% relative humidity experiment, minimum water vapor content in the lower layers of the model atmosphere is 2.5 times the threshold minimum value for which the parameterized equations are valid. Therefore, we feel that Fig. 9 is physically realistic. This suggests that the evolution of the temperature profile under nocturnal conditions is not nearly as sensitive to the exact water vapor profile for extremely cold conditions as it is for the more temperate situations encountered in midlatitudes, and as shown in the previous section.

In order to simulate properly the inversion development at Plateau Station, model runs have been made with the inclusion of the SBL, PBL and ground temperature parameterization schemes outlined previously. The 10 m level wind is assumed to be 5 m s^{-1}, which, using the similarity functions (12) and (13), yields the characteristic friction velocity u_* for each time step. Again, the initial temperature profile was assumed isothermal (230 K) in the lowest 1000 m and the model equations have been integrated for a 24-hour period. Three runs have been made using the same relative humidity profiles discussed earlier. As is revealed in Fig. 10, rapid cooling of the near surface layers occur during the first few hours of the model run, due primarily to longwave flux divergence. The outstanding feature in Fig. 10 is the short recovery time required for the inversion to reestablish. This is not unexpected. As discussed in Parish (1982), the presence of a temperature inversion over sloping terrain creates a pressure gradient force, which is the fundamental forcing mechanism for winds in the interior of Antarctica. These so-called "inversion winds" are known for their extreme persistence. Resultant wind calculations for various stations in the Antarctic interior show wind constancy values between 0.80 and 0.95. A rapid recovery of the inversion structure (and therefore the wind fields) after synoptic disruptions seems necessary to explain such extreme persistence.

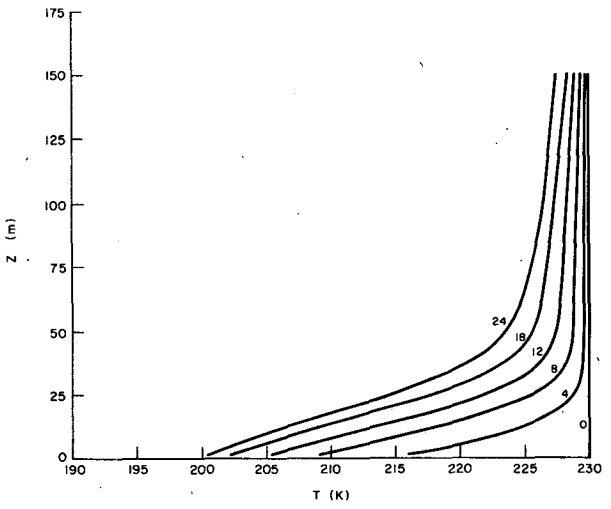

FIG. 10. Time evolution of the strong temperature inversion based on model calculations. Numbers refer to time in hours for representative temperature profiles.

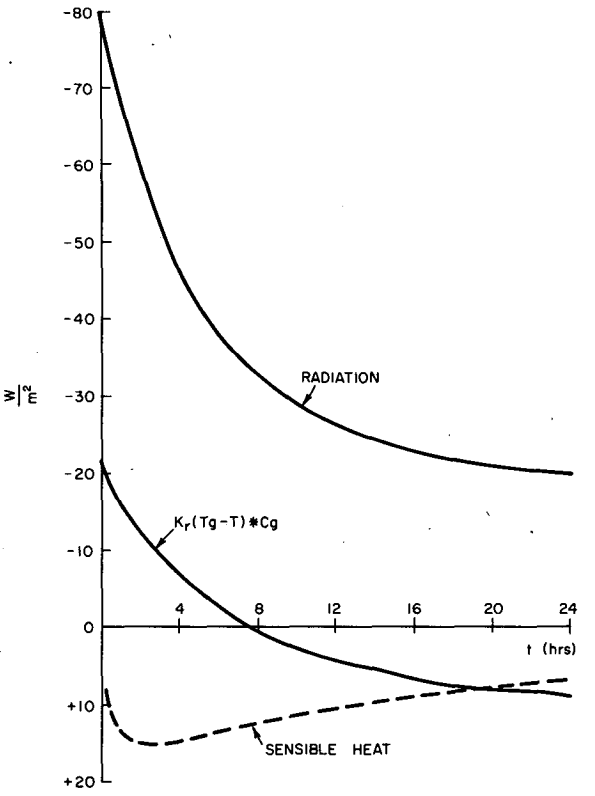

FIG. 11. Time-evolution of the various components of the surface energy budget.

The various components of the surface energy budget are illustrated in Fig. 11. Initially the longwave flux divergence is primarily responsible for the cooling. With time, the radiative cooling rate decreases rapidly, implying that the back radiation from the atmosphere approaches the value of the blackbody radiation upwards from the ground. The surface heat flux remains quite small throughout the model integration period in response to the relatively light surface winds and ever-increasing stability. As can be seen from Fig. 11, a steady-state situation at the surface is nearly achieved by 24 hours. Such an energy balance is discussed in Schwerdtfeger (1970) and can be used to explain the so-called "coreless" winter phenomenon. It has been observed that the temperature inversion

over the high interior of Antarctica does not increase throughout the dark winter months. Rather, a limiting inversion strength value of 30–40°C is achieved rapidly and a state of near balance between radiative cooling, turbulent heat flux and heat conduction through the snow/ice surface is attained, disrupted only by periods of cloudiness and wind associated with cyclonic storms. Results from the model simulation suggests near steady states can be reached in only a day or so.

The resulting temperature profiles after the 24-hour integration period are shown in Fig. 12. In each case, the inversion strength is on the order of 25–30°C. When reference is made to Fig. 9, it becomes apparent that the turbulent heat flux acts to diffuse the large vertical temperature difference over a substantially thicker layer as well as acting as a heat source at the surface. The resulting profiles are highly representative of the well-developed inversion structure documented frequently during the Plateau experiment. Comparison can be made with Fig. 13 from Schwerdtfeger (1970), showing average conditions for ten winter days during 1967 in which the cloud cover was less than 0.2 Ci. The surface winds for the averaging period ranged between 4 and 7 m s^{-1}, very representative of the gentle slopes in the Antarctic interior. For comparison, the 65% relative humidity model output from Fig. 12 is illustrated along with the Plateau Station temperature profile. As is obvious, the inversion structure displayed in Fig. 13 agrees well with the near steady-state model simulations presented in Fig. 12. It is concluded that the longwave graybody parameterization scheme presented in the previous section is capable of realistic simulations of the very stable temperature profile over the Antarctic interior, when combined with a qualitatively realistic turbulent heat diffusion scheme.

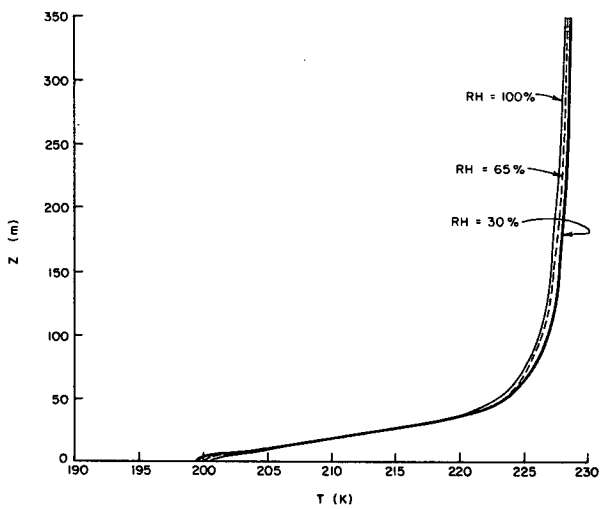

FIG. 12. Resulting temperature profile for varying relative humidities after 24-hour integration period.

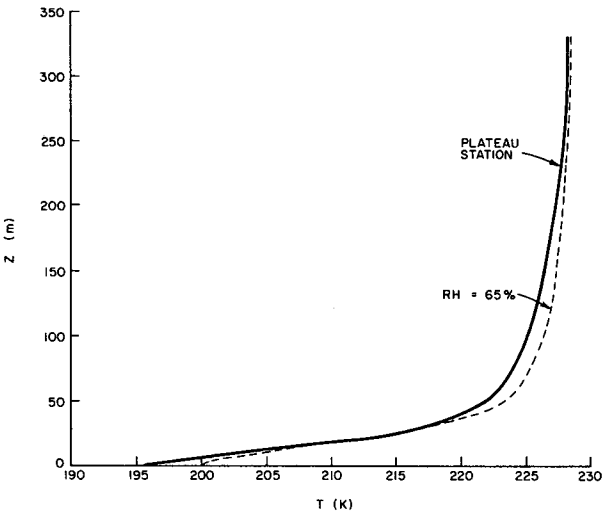

FIG. 13. The temperature inversion of Plateau Station, Antarctica based on average values of ten winter days in 1967 with cloudless sky or less than 0.2 Ci for which radio soundings and measurements along the 32 m micrometeorological tower are available. Surface winds during this period are between 4 and 7 m/s (from Schwerdtfeger, 1970). The 65% relative humidity model profile from Fig. 12 is superimposed for reference.

In the authors' opinion, accurate simulations of the temperature field over the high plateau of Antarctica are especially important for modeling of strong coastal katabatic flow (Parish, 1984). At present, the radiation parameterization scheme is being incorporated into a three-dimensional mesoscale model in order to investigate the spatial variability of katabatic flow along the Antarctic coast.

4. Conclusions

This paper presents a graybody, longwave, radiative transfer scheme that is computationally efficient and compares favorably in accuracy with more detailed radiative transfer models. The radiative transfer scheme presented here is suitable for the treatment of longwave radiation in primitive equation, climate and other comprehensive atmospheric models that demand significant computational time for the treatment of atmospheric dynamics. Three emissivity functions suitable for tropospheric modeling are presented. They include an emissivity for carbon dioxide, which is a function of temperature and pressure-corrected absorber amount, a second emissivity for the multiple water vapor bands and the H_2O–CO_2 overlap, which is a function of temperature and pressure corrected absorber amount, and a third emissivity for the water vapor continuum, which is a function of temperature and vapor pressure-corrected absorber amount. These new emissivity functions are compared with accepted emissivity values from the literature and differences are noted.

Radiative transfer model calculations are presented for high-, middle- and low-latitude model atmo-

spheres. Of particular note are the large cooling rates predicted near the surface in summer atmospheres. This feature is a result of the shape of the emissivity function for the water vapor continuum, including the vapor pressure weighting of corrected absorber amount, and will not be produced by older emissivity parameterizations.

The longwave radiative transfer scheme was augmented by a parameterization for turbulent heat transfer and a surface energy budget. The resultant one-dimensional atmospheric model was applied to the Antarctic winter and shown to produce realistic, surface temperature inversions such as those characterizing the interior of the Antarctic continent during the long polar night. The model predicts a dominance of longwave radiative cooling over other surface energy terms during the initial phases of inversion development. It also predicts that near equilibrium conditions are reached within 24 hours after cloudless skies and light wind conditions appear. The resulting inversion is 30°C over the lowest km, with most of the temperature difference occurring over the lowest 50 m. The prediction that the surface temperature inversion can reestablish itself within a few hours of a cloud deck passage or synoptic event supports the observed, extreme persistence of inversions in the interior of Antarctica. After 24 hours, very little additional development of the inversion is predicted, in agreement with the "coreless" winters observed in interior Antarctica. The radiatively forced, shallow temperature inversions in the Antarctic interior combined with the sloping terrain are believed to be the cause of persistent surface winds over the Antarctic hinterland.

Acknowledgments. The authors wish to thank S. S. Ou for providing multiple band model results plotted in Fig. 4. This research has been supported in part by the National Science Foundation through Grant DPP-8115976.

REFERENCES

Anthes, R. A., 1983: Regional models of the atmosphere in middle latitudes. *Mon. Wea. Rev.*, **111,** 1306–1335.

——, and T. T. Warner, 1978: Development of hydrodynamical models suitable for air pollution and other mesometeorological studies. *Mon. Wea. Rev.*, **106,** 1045–1078.

Blackadar, A. K., 1978: High resolution models of the planetary boundary layer. *Advances in Environmental and Scientific Engineering,* Vol. 1, Gordon and Breach, 50–85 pp.

Brost, R. A., and J. C. Wyngaard, 1978: A model study of the stably stratified planetary boundary layer. *J. Atmos. Sci.*, **35,** 1427–1440.

Businger, J. A., 1973: Turbulent transfer in the atmospheric surface layer. *Workshop on Micrometeorology,* D. A. Haugen, Ed., Amer. Meteor. Soc., 67–98.

——, J. C. Wyngaard, Y. Izumi and E. F. Bradley, 1971: Flux-profile relationship in the atmospheric surface layer. *J. Atmos. Sci.*, **28,** 181–189.

Elsasser, W. M., 1942: *Heat Transfer by Infrared Radiation in the Atmosphere.* Harvard Meteorological Studies No. 6, Harvard University Printing Office, Cambridge, 107 pp.

——, and M. F. Culbertson, 1960: *Atmospheric Radiation Tables. Meteor. Monogr.*, **4,** No. 23, Amer. Meteor. Soc., 1–43.

Kuhn, M., H. H. Lettaue and A. J. Riordan, 1977: Stability related wind spiraling in the lowest 32 m. Meteorological studies at Plateau Station, Antarctica, Pap. 7, *Antarctic Research Series,* Vol. 25, Amer. Geophys. Union, 93–111.

Lettau, H. H., 1966: A case study of katabatic flow on the south polar plateau. Studies in Antarctic Meteorology, *Antarctic Res. Series,* Vol. 9, Amer. Geophys. Union, 1–11.

——, 1979: Wind and temperature profile prediction for diabatic surface layers including strong inversion cases. *Bound.-Layer Meteor.*, **17,** 443–464.

——, A. J. Riordan and M. Kuhn, 1977: Air temperature and two-dimensional wind profiles in the lowest 32 meters as a function of bulk stability. Meteorological Studies at Plateau Station, Antarctica, Pap. 6, *Antarctic Res. Series,* Vol. 25, Amer. Geophys. Union, 77–91.

Liou, K., 1980: *An Introduction to Atmospheric Radiation.* Academic Press, 392 pp.

——, and S. S. Ou, 1981: Parameterization of infrared radiative transfer in cloudy atmospheres. *J. Atmos. Sci.*, **38,** 2707–2716.

——, and ——, 1983: Theory of equilibrium temperatures in radiative-turbulent atmospheres. *J. Atmos. Sci.*, **40,** 214-229.

McClatchey, R. S., R. W. Fenn, J. E. Selby, F. E. Volz and J. S. Gainge, 1972: *Optical Properties of the Atmosphere, 3rd ed.* AFCRL-72-0497, 113 pp.

McNider, R. T., and R. A. Pielke, 1981: Diurnal boundary layer development over sloping terrain. *J. Atmos. Sci.*, **38,** 2198–2212.

Mahrer, Y., and R. A. Pielke, 1977: The effects of topography on the sea and land breezes in a two-dimensional numerical model. *Mon. Wea. Rev.*, **105,** 1151–1162.

Mahrt, L. J., and W. Schwerdtfeger, 1970: Ekman spirals for exponential thermal wind. *Bound.-Layer Meteor.*, **1,** 137–145.

Mather, K. B., and G. S. Miller, 1966: Wind drainage off the high plateau of eastern Antarctica. *Nature,* **209,** 281–284.

Ou, S. S., and K. Liou, 1983: Parameterization of carbon dioxide 15 μm band absorption and emission. *J. Geophys. Res.*, **88,** 5203–5207.

Parish, T. R., 1982: Surface airflow over East Antarctica. *Mon. Wea. Rev.*, **110,** 84–90.

——, 1984: A numerrical study of strong katabatic winds over Antarctica. *Mon. Wea. Rev.*, **112,** 545–554.

Radok, U., and R. C. Lile, 1977: A year of snow accumulation at Plateau Station. Meteorological Studies at Plateau Station, Antarctica, Pap. 2, *Antarctic Res. Series,* Vol. 25, Amer. Geophys. Union, 17–26.

Riordan, A. J., 1977: Variations of temperature and air motion in the 0- to 32-meter layer at Plateau Station, Antarctica. Meteorological Studies at Plateau Station, Antarctica, Pap. 8, *Antarctic Res. Series,* Vol. 25, Amer. Geophys. Union, 113–127.

Roberts, E., J. E. Selby and I. M. Biberman, 1976: Infrared continuum absorption by atmospheric water vapor in the 8–12 μm window. *Appl. Opt.*, **15,** 2085–2090.

Rodgers, C. D., and C. D. Walshaw, 1966: The computation of infrared cooling rate in planetary atmospheres. *Quart. J. Roy. Meteor. Soc.*, **93,** 43–54.

Roewe, D., and K. Liou, 1978: Influence of cirrus clouds on the infrared cooling rate in the troposphere and lower stratosphere. *J. Appl. Meteor.*, **17,** 92–106.

Sasamori, T., 1968: The radiative cooling calculation for application to general circulation experiments. *J. Appl. Meteor.*, **7,** 721–729.

——, 1972: A linear harmonic analysis of atmospheric motion with radiative dissipation. *J. Meteor. Soc. Japan,* **50,** 505–518.

Schwerdtfeger, W., 1970. *The Climate of the Antarctic,* Vol. 14, S. Orvig, Ed., *World Survey of Climatology,* H. E. Landsberg, Ed., Elsevier, 253–355.

Staley, D. O., and G. M. Jurica, 1970: Flux emissivity tables for water vapor carbon dioxide and ozone. *J. Appl. Meteor.*, **9,** 365–372.

Yamamoto, G., 1952: On a radiation chart. Sci. Rep. Tohoku University, Ser. 5 (Geophysics), **4,** 9–23.